Fast Circuit Simulation of Power Electronic Circuits Using Modified Nodal Analysis

N. Voyer, A. Nakabayashi, and R. Kondo, *Senior Member, IEEE*

***Abstract*—This article introduces a method that reaches the closed-form expression of waveforms in linear electronic circuits, enabling fast and accurate simulations. The method is automated for circuits described with modified nodal analysis formalism, that is easy to reach with collection of Kirchhoff laws. The method produces same closed-form expressions of waveforms as in state-space analysis (SSA), expressed as sums of weighted exponential functions of time, driven by characteristic frequencies of the circuit. However, the proposed method does not use SSA formalism and can therefore be applied to any circuit. The precise formulation of waveforms enables its computation in a single step with ultimate accuracy and constant CPU effort. Significant acceleration ratio was verified on dc/dc circuit by comparison with commercial simulation tool. Methodology is also applied to the simulation of motor drive circuits. The proposed method can effectively reduce the calculation effort at the design and verification stages of applications which need loss analysis over long mission profiles, like mobility applications.**

***Index Terms*—Electronic circuits, modified nodal analysis (MNA), simulation, state-space analysis (SSA).**

I. Introduction

SIMULATION-BASED design of e-mobility power electronic converters involves a very large number of simulations at various scales, that gets further amplified by the necessity to check the control interactions across successive conversion stages and across evolving drive conditions. Key performance indicators, such as losses, temperature, and stabilization of control waveforms must be verified and/or optimized over a large design space of circuit and control parameters. Each design of each converter must be verified across the many operating conditions met during the various desired missions of the application [1], [2], [3], [4]. To deal with such a high number of simulations, the execution speed of simulation becomes crucial. Speed of execution and the related computing resource is also critical for other applications (e.g., virtual twin, model-predicted control, simulation/hardware-in-the-loop), which must run simulation faster than in real-time, in parallel to the real converter.

Received 28 April 2025; revised 25 June 2025 and 5 August 2025; accepted 27 August 2025. Date of publication 29 August 2025; date of current version 13 November 2025. Recommended for publication by Associate Editor C. Tse. *(Corresponding author: N. Voyer.)*

N. Voyer is with Mitsubishi Electric Research Centre Europe, 35708 Rennes, France (e-mail: n.voyer@fr.merce.mee.com).

A. Nakabayashi and R. Kondo are with Mitsubishi Electric Corporation, Amagasaki 661-8661, Japan.

Color versions of one or more figures in this article are available at https://doi.org/10.1109/TPEL.2025.3604213.

Digital Object Identifier 10.1109/TPEL.2025.3604213

For simulation over long mission profiles, electrothermal averaged model significantly relaxes the simulation effort by means of steady-state formulation of converter, skipping the simulation of switching transients, of current ripples and of controller-circuit interactions [20]. Neglecting current ripple however biases the estimation of switching losses. To replicate with accuracy the switching currents and the corresponding losses for each switching device, simulation must address current ripple and replicate pulsewidth modulation (PWM) operation.

For a given circuit model, the speed of simulation generally relates to the level of expected computation accuracy (or tolerance). In modified nodal analysis (MNA) approach, the differential equations of circuit waveforms, derived from the collection of Kirchhoff laws, are generally solved in literature [5], [6], [7], [8], [9], [10] locally as linear or polynomial functions of time and evaluated over consecutive simulation steps. Polynomial solvers fundamentally control the accuracy through appropriate step size and approximation order, meaning that they are inaccurate by principle, with the risk of cumulating inaccuracies over long simulation scenarios. To limit this risk, the accuracy of simulation is driven by an appropriate choice of simulation step and polynomial order, at the price of CPU complexity.

In contrast, approximation-free closed-form expression of waveforms is possible for linear time invariant (LTI) circuits which can get represented by means of state-space analysis (SSA) [11], [12]. SSA formalism yields precise formulation of circuit waveforms as weighted sum of exponential functions of time, which polynomial time series expansion have infinite number of terms. Being free of truncation error, SSA solvers can realize event-driven simulation, where the simulation step is enlarged to the interval between simulation events (sampling, switching), skipping the simulation of circuit waveforms at intermediate timesteps. Reaching SSA formalism for any kind of electronic circuit is however not straightforward and SSA cannot automatically be applied for any circuit topology. Relations between MNA and SSA formalisms were investigated over special cases [14], [15], [16].

The closed-form expression of LTI circuit waveforms was recently shown to be reachable from MNA formalism, using the built-in symbolic ODE solver available in Maple software [17]. The method however hides the underlying analytical developments and lacks a proof of general applicability. A clear method was recently introduced [19] that systematically reaches the precise closed-form expression of linear circuit waveforms, starting

from MNA representation of any LTI circuit. The proposed fast circuit simulator (FCS) method combines the advantages of both MNA and of SSA solvers: applicability to any circuit topology using Kirchhoff equations, approximation-free results with minimal complexity using closed-form expression.

When analyzing nonlinear circuits with SSA, closed-form solutions unfortunately no longer apply and truncated polynomials must be used, as explored in [13] for the simulation of motor drive applications. While FCS was initially only investigated for static converters, the present article aims at extending the applicability of MNA closed-form expressions to more complex circuits including motor drives.

The rest of this article is organized as follows. Section II first recalls the mathematical equations of MNA and SSA formalisms for static electric circuits and the closed-form expression of waveforms reachable by SSA. Section III develops the similar closed-form waveform formulation reached by FCS. Section IV then addresses the usage of FCS in circuit composed of active devices driven by a circuit controller. Applicability of FCS to motor drive circuits is then explored and discussed in Section V. Section VI examines performance of simulation for traction drive application, composed of dc/dc step up converter and an inverter driving a salient permanent magnet synchronous machine (PMSM). Finally, Section VII concludes this article, discussing the applicability and the foreseen limits of the proposed methodology.

II. MNA and SSA Formalisms

A. Modified Nodal Analysis

An electronic circuit consisting of N_b branches and N_n nodes is analyzed in this section. Considering that the last node of the circuit is grounded, the electrical circuit exhibits $N_w = N_b + N_n - 1$ circuit waveforms, collected in waveform vector $\vec{x}$

$$\vec{x}(t) = \left(V_1, \ldots, V_{N_n-1}, i_1, \ldots, i_{N_b}\right)^T. \tag{1}$$

Branch impedance analysis yields N_b branch voltage relations as function of branch current. Kirchhoff law of currents brings $N_n - 1$ independent additional current balance relations. From the collected set of N_w equations, the dynamics of the circuit are then represented by an equation system

$$\boldsymbol{C}.\dot{\vec{x}}(t) + \boldsymbol{G}.\vec{x}(t) = \vec{u}(t) \tag{2}$$

where $\vec{u}(t)$ is the input power source vector representing the input power source of each branch. The merit of MNA framework is that the $N_w \times N_w$matrices $\boldsymbol{C}$ and $\boldsymbol{G}$ can get automated from the description of the circuit. The matrix $\boldsymbol{C}$ contains inductance or capacitance values of each branch of the circuit, while matrix $\boldsymbol{G}$ contains resistance values of each branch, as well as sign conventions for currents of branches connected to each node of the circuit.

For a circuit comprising N_C capacitors and N_L inductors, the energy state of the circuit is represented by the state vector $\vec{X}$ of size $N_P = N_C + N_L$

$$\vec{X}(t) = \left(V_{C_1}, \ldots, V_{C_{N_C}}, I_{L_1}, \ldots, I_{L_{N_L}}\right)^T. \tag{3}$$

The state vector $\vec{X}(t)$ also relates to the waveform vector $\vec{x}(t)$ through a simple and easy to determine matrix relation

$$\vec{X}(t) = \boldsymbol{K}.\vec{x}(t) \tag{4}$$

where $\boldsymbol{K}$ is a $N_P \times N_w$ matrix filled with values in $\{-1, 0, 1\}$. Collecting first the voltage equations of branches containing passive energy storage components (inductances, capacitances), MNA formulation (2) can be driven to have

$$\boldsymbol{C} = \begin{bmatrix} \boldsymbol{\Delta}.\boldsymbol{K} \\ 0 \end{bmatrix} \tag{4b}$$

where $\boldsymbol{\Delta}$ is a $N_P \times N_P$ diagonal matrix containing values of inductances and capacitances.

B. Truncated Taylor-Series Approximation

The MNA system represented by (2) can be numerically solved, using polynomial approximation. The waveform vector is searched under a polynomial form with coefficient vectors $\{\overrightarrow{b_k}\}_{k \le K}$

$$\vec{x}(t) = \sum_{k=0}^{\infty} \overrightarrow{b_k}.t^k = \sum_{k=0}^{K} \overrightarrow{b_k}.t^k + \vec{o}\left(t^K\right). \tag{5}$$

The derivation of waveform vector is then expressed as

$$\dot{\vec{x}}(t) = \sum_{k=0}^{K-1} (k+1).\overrightarrow{b_{k+1}}.t^k + \vec{o}\left(t^{K-1}\right). \tag{6}$$

The resolution must start from the initial conditions observed on passive energy storage components of the circuit, bringing N_P relations for N_w unknowns on vector $\overrightarrow{b_0}$

$$\vec{X}(0) = \boldsymbol{K}.\overrightarrow{b_0}. \tag{7}$$

Other missing relation terms may be found through recursive identification of polynomial terms arising from (2). Identification on the kth order each time adds N_w new relations and N_w new unknowns on vector $\overrightarrow{b_{k+1}}$

$$(k+1).\boldsymbol{C}.\overrightarrow{b_{k+1}} + \boldsymbol{G}.\overrightarrow{b_k} = \overrightarrow{u_k} \tag{8}$$

where input power source term $\vec{u}\ (t) = \sum_{k=0}^{\infty} \overrightarrow{u_k}.t^k$ is represented by its Taylor-series expansion. Eventually, this builds a linear system with $(kN_w + N_P)$ relations with $(k+1)N_w$ unknowns. The apparent lack of relations can be resolved by neglecting highest order, and by setting $N_w - N_P$ terms to zero in the last $\overrightarrow{b_{k+1}}$ expression. The accuracy is driven by the term $\vec{o}(t^K)$, which is a function of approximation order K and of step size t and is approximated as

$$\left\|\vec{o}\left(t^K\right)\right\| \cong \left\|\overrightarrow{b_{k+1}}\right\|.t^{K+1}. \tag{9}$$

The complexity of the linear system to be inverted increases with the approximation order.

As seen in Fig. 1, approximating a sine function over a duration of one or multiple periods with a polynomial requires quite large polynomial orders. The added complexity brought by higher order approximation may thus not always guarantee a significant complexity gain compared with using smaller steps.

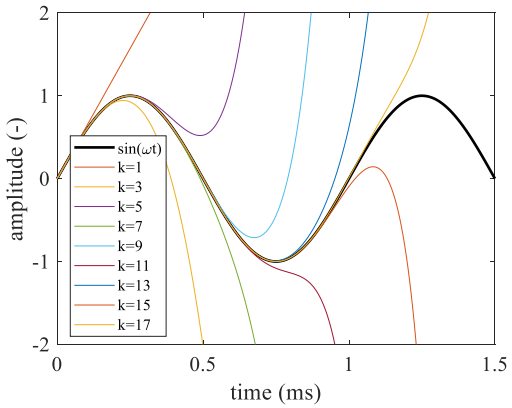

Fig. 1. Approximation of a 1000 Hz sine function by truncation at different orders of Taylor polynomial expansion.

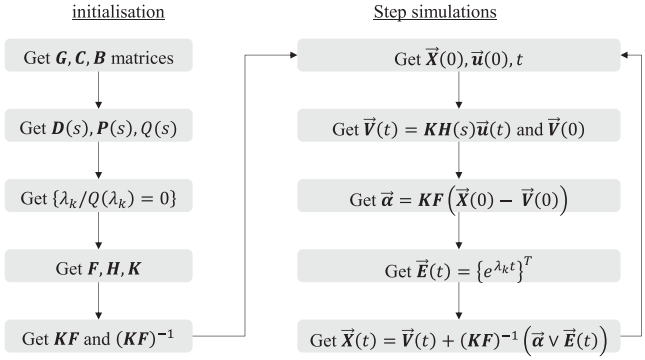

Fig. 2. Workflow of proposed fast circuit solver.

C. Solution Formulation With State-Space Analysis

In SSA framework [11], [12], [17], the state vector relates to its derivatives according to

$$\dot{\vec{X}}(t) = \boldsymbol{A}_{\text{SSA}}.\vec{X}(t) + \vec{U}(t) \tag{10}$$

where $\boldsymbol{A}_{\text{SSA}}$ is a full-rank $N_p \times N_p$ matrix, and $\vec{U}(t)$ is representative of the input power source vector $\vec{u}(t)$.

From (10), and assuming constant power sources $\vec{U}(t) = \vec{U}$, the solution elegantly comes as

$$\vec{X}(t) = -\boldsymbol{A}_{\text{SSA}}{}^{-1}.\vec{U} + \sum_i \alpha_i.e^{\lambda_i t}.\vec{V}_i \tag{11}$$

where $\{\lambda_i\}_{i\leq N_P}$ are eigenvalues of matrix $\boldsymbol{A}_{\text{SSA}}$ identified as characteristic frequencies of electrical circuit, and $\vec{V}_i, i \leq N_P$ are corresponding eigenvectors of matrix $\boldsymbol{A}$, i.e., $\boldsymbol{A}_{\text{SSA}}.\vec{V}_i = \lambda_i.\vec{V}_i$.

The weights $\{\alpha_i\}_{i\leq N_P}$ are identified from initial conditions

$$\vec{X}(0) = -\boldsymbol{A}_{\text{SSA}}{}^{-1}.\vec{U} + \sum_i \alpha_i.\vec{V}_i \tag{12}$$

$$\vec{\alpha} = \boldsymbol{V}^{-1}.\left(\vec{X}(0) + \boldsymbol{A}_{\text{SSA}}{}^{-1}.\vec{U}\right) \tag{13}$$

where $\boldsymbol{V}$ is a matrix gathering eigenvectors of matrix $\boldsymbol{A}_{\text{SSA}}$. The weight vector $\vec{\alpha}$ is thus determined from (13), enabling the identification of state vector $\vec{X}(t)$ at any time instant with (11).

Using (2), (4) and (11), considering that $\boldsymbol{G}$ is of full rank, the expression of full waveform vector is ultimately reached

$$\vec{x}\ (t) = \boldsymbol{G}^{-1}.\left(\vec{u}\,(t) - \begin{bmatrix}\boldsymbol{\Delta}.\dot{\vec{X}}(t)\\ 0\end{bmatrix}\right) \tag{14}$$

where

$$\dot{\vec{X}}(t) = -\boldsymbol{A}_{\text{SSA}}{}^{-1}.\dot{\vec{U}} + \sum_i \alpha_i.\lambda_i.e^{\lambda_i t}.\vec{V}_i. \tag{15}$$

The formal solution (15) brought by SSA thus allows the computation of waveforms at any time with perfect accuracy. SSA has great benefit of absence of any approximation, and repeatable CPU complexity that is independent of initial conditions of the circuit.

The approximated MNA solver is thus more complex than the SSA solver, and less accurate. However, translating MNA equation system into SSA is not a trivial task and could not yet be generalized especially for circuits with a large number of circuit branches.

III. Fast Circuit Solver

The fast circuit solver (FCS) presented in this section addresses static circuits, composed of *RLC* components and variable power sources. The proposed framework is equally applicable for circuits with transformers (e.g., CIC, LLC, DAB) or waveform-controlled power sources (e.g., transconductance of power device), as long as circuits be described with linear MNA formulation (2).

A. Overall Solver Workflow

Fig. 2 depicts the general workflow of the proposed FCS. An initialization stage gathers computation steps that are independent of circuit state. This includes the identification of MNA matrices $\boldsymbol{C}$ and $\boldsymbol{G}$, a triangulation of the related Laplace matrix $\boldsymbol{A}_{\text{MNA}}(s)$ using two Gauss–Jordan elimination steps, the identification of a vector characteristic frequencies $\vec{\lambda}$, the determination of a filter matrix $\boldsymbol{K}.\boldsymbol{H}$ of input power sources, and the determination and the inversion of a matrix $\boldsymbol{K}.\boldsymbol{F}$ of weights of transfer functions. The simulation step determines a vector $\vec{V}$ of filtered functions of power sources, a weight vector $\vec{\alpha}$, and characteristic functions of time $\vec{E}(t)$ and finally the circuit waveforms $\vec{X}(t)$ at any instant t from the initial conditions of passive components $\vec{X}(0)$. The complexity of the simulation step is independent of the time at which the waveforms must be computed.

B. Notations and Lower-Upper (LU) Decomposition

MNA (2) can get rewritten as

$$\boldsymbol{A}_{\text{MNA}}(s).\vec{x}(t) = \vec{u}(t) \tag{16}$$

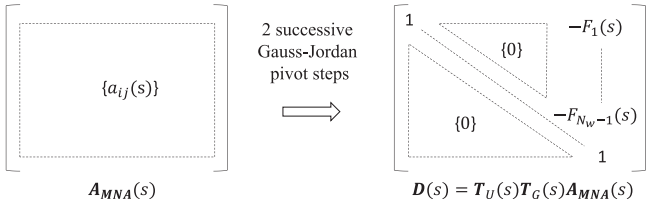

Fig. 3. MNA matrix of transfer function $\boldsymbol{A}_{\text{MNA}}(s)$ is modified with two successive Gauss-Jordan elimination steps with matrices $\boldsymbol{T_U}(s)$ and $\boldsymbol{T_G}(s)$. Final matrix $\boldsymbol{D}(s)$ is identity matrix with nonzero elements on its last column.

where $\boldsymbol{A}_{\text{MNA}}(s) = \boldsymbol{G} + \boldsymbol{C}s$ is a matrix of transfer functions, and s is the Laplace operator: $s^k.x(t) = \partial^k/\partial t^k(x(t))$. Considering $\boldsymbol{A}_{\text{MNA}}(s)$ is of full rank, a first Gauss-Jordan elimination step is applied. Using pivotal matrix $\boldsymbol{T_G}(s)$, we get

$$\boldsymbol{B}(s).\vec{x}(t) = \boldsymbol{T_G}(s).\vec{u}(t) \tag{17}$$

where $\boldsymbol{B}(s) = \boldsymbol{T_G}(s).\boldsymbol{A}_{\text{MNA}}(s)$ is an upper triangular matrix of transfer functions, with $b_{i,j}\ (s) = 0\ (\forall j, \forall i > j)$, and unity diagonal terms: $\forall i, b_{i,i}\ (s) = 1$.

As also shown in Fig. 3, a second partial Gauss–Jordan elimination step is then applied. Using upper triangular matrix $\boldsymbol{T_U}(s)$, we get

$$\boldsymbol{D}(s).\vec{x}(t) = \boldsymbol{T_U}(s).\boldsymbol{T_G}(s).\vec{u}(t) \tag{18}$$

where $\boldsymbol{D}(s) = \boldsymbol{T_U}(s).\boldsymbol{T_G}(s).\boldsymbol{A}_{\text{MNA}}(s)$ is still an upper triangular matrix of transfer functions, with $d_{i,j}\ (s) = 0\ (\forall i < N_w, \forall j \neq i)$, and unity diagonal terms : $\forall i, d_{i,i}(s) = 1$, zero terms elsewhere $d_{i,j}\ (s) = 0$, $(\forall j,\ i < j < N_w)$, except on the last column, where $d_{i,N_w}(s) = -F_i(s) \neq 0\ (\forall i < N_w)$. Unlike traditional LU decomposition, the second Gauss-Jordan elimination is applied on the $N_w - 1$ first dimensions only, preserving transfer relations between the last waveform and all other waveforms in the circuit. Some terms $F_i(s)$ on the last column could be zero if the electronic circuit can be severed into disjoint subcircuits, in which case waveforms of one subcircuit cannot get interrelated to waveforms of other subcircuits. For circuits that cannot be reduced into disjoint subcircuits, all circuit waveforms are interrelated with nonzero transfer functions, and $F_i(s)$ represents the transfer function between each *i*th waveform and the last waveform of circuit waveform vector $\vec{x}(t)$. Gains $F_i(s)$ are analogue to the Mason's gains applied to the signal flow graph of the circuit [18].

C. Identification of Characteristic Frequencies

On its last dimension, (18) expresses the last waveform as

$$x_{N_w}(t) = \sum_k T_{G,N_w,k}(s).u_k(t). \tag{19}$$

By pivotal construction, $T_{G,N_w,k}(s)$ is a transfer function, equal to a ratio of s polynomials

$$T_{G,N_w k}(s) = \frac{P_{N_w,k}(s)}{Q(s)}. \tag{20}$$

Equation (19) can thus be reduced to the following ordinary differential equation (ODE) driven by characteristic polynomial $Q(s)$, the common denominator of matrix $\boldsymbol{T_G}(s)$

$$Q(s).(x_{N_w}(t) - y(t)) = 0 \tag{21}$$

where $y\ (t) = \sum_k P_{N_w,k}(s).u_k(t)$. The last waveform $x_{N_w}(t)$ thus necessarily takes the following formal expression of time:

$$x_{N_w}(t) = y(t) + \sum_k \alpha_k.e^{\lambda_k t} \tag{22}$$

where $\vec{\alpha} = \{\alpha_k\}$ is a vector of complex weights and $\{\lambda_k\}$ are the characteristic frequencies of the circuit, identified as complex roots of the characteristic polynomial $Q(s)$

$$Q(\lambda_k) = 0. \tag{23}$$

For high polynomial orders, finding symbolic solutions to characteristic frequencies from (23) is not always possible. Polynomial roots can however get identified digitally using e.g., native potentially CPU-intensive MATLAB routine.

D. Intermediate Formulation of Circuit Waveforms

When the circuit is not built of independent subcircuits, the terms $F_i(s)$ are not zero: each *i*th waveform is related to the last waveform $x_{N_w}(t)$ through a transfer function $F_i(s)$. For the sake of notations, the canonical vector $\vec{\delta_i}$ is introduced $(\vec{\delta}_i(i) = 1,\ \vec{\delta}_i(j \neq i) = 0)$ to reach

$$x_i(t) = F_i(s).x_{N_w}(t) + \vec{\delta}_i.\boldsymbol{T_U}(s).\boldsymbol{T_G}(s).\vec{u}(t). \tag{24}$$

From (22) and identification of characteristic components in (24), the expression of each circuit waveform can be reached

$$x_i(t) = \sum_{k \leq N_P} \alpha_k.F_i(\lambda_k).e^{\lambda_k t} + v_i(t) \tag{25}$$

where $v_i(t)$ are filtered functions of input power sources and transfer function $\boldsymbol{H}_i(s)$ of corresponding filters are expressed as

$$v_i(t) = \boldsymbol{H}_i(s).\vec{u}(t) \tag{26}$$

$$\boldsymbol{H}_i(s) = \left(\vec{\delta}_i + F_i(s).\vec{\delta}_{N_w}\right).\boldsymbol{T_U}(s).\boldsymbol{T_G}(s). \tag{27}$$

E. Filtered Function of Example Power Sources

By construction (27), transfer functions of filters are determined as ratios of polynomial transfer functions

$$\boldsymbol{H}_i(s) = \frac{\boldsymbol{P}_i(s)}{Q(s)} = \frac{\sum_k \boldsymbol{p}_{ik}s^k}{\sum_k q_k s^k}. \tag{28}$$

When power source is sinusoidal with time, then filtered functions $v_i(t)$ are also oscillating with same frequency but different amplitude and phase

$$\vec{u}(t) = \boldsymbol{\mathcal{R}}\left(e^{j\omega t+\phi}\right).\vec{U}_0, \tag{29}$$

$$v_i(t) = \boldsymbol{\mathcal{R}}\left(e^{j\omega t+\phi}.\boldsymbol{H}_i\left(j\omega\right).\vec{U}_0\right). \tag{30}$$

When power source is linear with time

$$\vec{u}(t) = \vec{U}_0 + \vec{U}_1.t. \tag{31}$$

Then, if $q_0 \neq 0$, $v_i(t)$ is also linear with time $v_i\ (t) = V_{i0}\ + V_{i1}.t$

$$\begin{cases} V_{i1} = \frac{\boldsymbol{p}_{i0}}{q_0}.\vec{U}_1 \\ V_{i0} = \frac{\boldsymbol{p}_{i0}}{q_0}.\vec{U}_0 + \frac{q_0.\boldsymbol{p}_{i1} - q_1.\boldsymbol{p}_{i0}}{{q_0}^2}.\vec{U}_1 \end{cases}. \tag{32}$$

Some derated cases may occur with $q_0 = 0$: as example when a capacitor is connected in series with a current source, or when an inductance is connected in parallel to a voltage source. Then $v_i(t)$ gets quadratic with time $v_i(t) = V_{i1}.t + V_{i2}.t^2$

$$\begin{cases} V_{i2} = \frac{\boldsymbol{p}_{i0}}{q_1}.\vec{U}_1 \\ V_{i1} = \frac{\boldsymbol{p}_{i0}}{q_1}.\vec{U}_0 + \frac{q_1.\boldsymbol{p}_{i1} - q_2.\boldsymbol{p}_{i0}}{{q_1}^2}.\vec{U}_1 \end{cases}. \tag{33}$$

Nevertheless, it is possible to always avoid derated cases, simply adding artificial (large) resistances R_ϵ in parallel to capacitors, and (small) in series to inductors. With an appropriate choice of each resistance R_ϵ, the resulting time constants $\tau_C = R_\epsilon\ C$, $\tau_L = L/R_\epsilon$ is significantly higher than the simulation step time (e.g., switching period), and eventually the associated inaccuracy brought by adding artificial resistance is limited to a desired level t/τ_C.

F. Identification of Weights From Initial Conditions

Waveforms of energetic passive components $\vec{X}(0) = \boldsymbol{K}.\vec{x}(0)$ are known at initial time t = 0. Introducing a matrix $\boldsymbol{F} = \{F_{ij} = F_i(\lambda_j)\}$, and noting $\vec{V}(t) = \boldsymbol{K}.\vec{v}(t)$, where $\vec{v}(t) = (v_1(t), \ldots, v_{N_w}(t))^T$, initial conditions are expressed as

$$\vec{X}(0) = \boldsymbol{K}.\vec{x}(0) = \boldsymbol{K}.\boldsymbol{F}.\vec{\alpha} + \vec{V}(0). \tag{34}$$

Eventually, the weight vector $\vec{\alpha}$ is identified from

$$\vec{\alpha} = (\boldsymbol{K}.\boldsymbol{F})^{-1}.\left(\vec{X}(0) - \vec{V}(0)\right). \tag{35}$$

It should be noted here that the matrix $(\boldsymbol{K}.\boldsymbol{F})$ to get inverted is independent of initial circuit conditions and of dimensions $N_P \times N_P$, equal to that of SSA formulation, and of much reduced complexity compared with the $N_w \times N_w$ dimension of matrix $\boldsymbol{G}$ of initial MNA problem expressed from (9). Some derated cases may occur when $(\boldsymbol{K}.\boldsymbol{F})$ is singular and cannot get inverted. This occurs as example when capacitors are connected in parallel, or inductors are connected in series and therefore share the same transfer function $F_i(s)$. Such derated case can get avoided by simplification of circuit, merging the parallel capacitors or the series-connected inductances into a single component.

G. Final Formulation of Waveforms

Once weight vector $\vec{\alpha}$ is identified, the waveform vector is identified from (25) as

$$\vec{x}(t) = \vec{v}(t) + \boldsymbol{F}.\left(\vec{\alpha} \vee \vec{E}\,(t)\right) \tag{36}$$

where $\vec{E}\ (t) = (e^{\lambda_1 t}, \ldots, e^{\lambda_{N_P} t})^T$ are characteristic functions of time of the circuit, identified by characteristic frequencies $\{\lambda_k\}$. $\vee$ is the term-by-term product operator. Using (4), state vector becomes

$$\vec{X}(t) = \vec{V}(t) + \boldsymbol{K}.\boldsymbol{F}.\left(\vec{\alpha} \vee \vec{E}\,(t)\right). \tag{37}$$

The final expressions (36) and (37) are very similar to (14) and (11), but required no identification of SSA framework, nor eigenvector analysis of SSA matrix. MNA and SSA frameworks lead to the same analytical solution, built with identical exponential characteristic functions: they are both equally precise, for any time instant, and without approximation/truncation of polynomial solution. The proposed analysis is furthermore applicable to any input power sources.

H. Nonlinear Circuits

In nonlinear circuits, some circuit parameters evolve as function of circuit waveforms. Assuming local stability of parameter value, the FCS strategy might be applied in-between consecutive simulation events. At each simulation event, the circuit waveforms are updated together with circuit parameters. In contrast to simulation of LTI circuits, the initialization stage, including the triangulation, the identification of characteristic frequencies, the computation and inversion of matrix $(\boldsymbol{K}.\boldsymbol{F})$ must then get recomputed.

Considering the CPU costs associated to the initialization stage and the inaccuracy induced by the local stability assumption, FCS does not seem very attractive for the simulation of nonlinear circuits, which therefore were not addressed in the present article.

IV. Circuits With Active Devices

A. Ideal Switch Concept

Modern power electronic designs generally also comprise switching devices, such as diodes or transistors. In these circuits, the circuit state changes together with the conduction or the blocking state of its switching components. After switching transients, the circuit derates into *RLC* subcircuits, which can be analyzed with the proposed FCS method.

Switching transients observed in double pulse tests (DPTs) carry information on switching losses and EMC emissions, and occur at nanoseconds scale, especially for wide bandgap devices (SiC, GaN). This time scale is generally small with respect to the precision of PWM (few hundreds of nanoseconds), and to the deadtime (few microseconds or less) applied to top and bottom switches of half bridges. Switching transient results also describe the voltage overshoot and the associated current ringing associated to the EMC emissions of the converter. The switching transients may get replicated in detail by means of analytic models described as lumped elements equivalent circuit, which comprises ideal switches, parasitic *RLC* components, waveform-controlled power source (transconductance) and e.g., nonlinear Miller or output capacitance. Such simulations involve nanosecond-scale precision, hardly compatible with the objective of reduction of CPU simulation effort. While in principles, the proposed FCS might be used for the simulation of such models, this was not explored in this article due to the very nonlinear nature of the associated circuit parameters. In

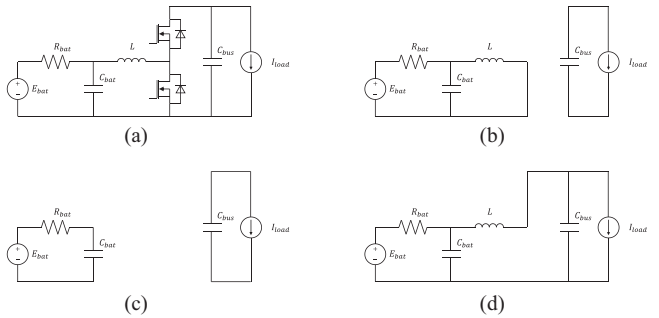

Fig. 4. Decomposition of boost converter circuit. (a) Into disjoint subcircuits for each half-bridge state. (b) Bottom-side connected. (c) Disconnected. (d) Top-side connected.

practice, the accuracy of transient simulation models is always questionable and reliable DPT results are preferably built from measurement instead of simulation. DPT results are assumed available beforehand for each switching condition (voltage, current, gate resistance, and junction temperature).

Using ideal switches in the simulation of power converter over complex long mission profiles can relax the simulation effort, as switching losses and EMC emissions can be later be accounted for using lookup tables, such as loss maps where switching losses are functions of arm current and bus voltage, of gate circuit parameters (e.g., gate resistance and low/high gate voltages) and/or of junction temperature.

The scheme can be adapted to any technique for loss verification but will rely on the accuracy of loss estimation. As example loss map may be built with high accuracy from the DPT results measured with calorimeter. For wide bandgap device with high *dV/dt* gate control, it is not recommended to estimate the losses from voltage/current DPT waveforms, due to (bandwidth/delay) limitations in market available probes and oscilloscopes.

B. Circuit / Controller Interactions

The active devices (IGBTs, MOSFETs) being modelled as ideal switches, the circuit topology evolves dynamically according to the conduction state of circuit switches, as shown in Fig. 4 for a simple dc/dc boost circuit example. For a given switching state, the circuit derates into one or several independent subcircuits built of only passive and power source elements, as nonconductive switches get removed from the circuit, and conductive switches are replaced with shortcut current paths. At initialization stage, FCS initialization is run for all subcircuits of all possible states of the circuit. The associated relatively CPU-consuming tasks are realized only once. At simulation stage, the circuit simulator must operate in coordination with one or more circuit controller. Circuit controller takes as input some waveform data sampled at precise ADC sampling events, and then determines the timing of next switching and next ADC events. As an example, the circuit controller decides switching events according to PWM, by comparison of a triangular PWM carrier and desired modulating voltage, and the timing of ADC events are aligned with the edges of PWM carrier.

C. Transitions Between Circuit States

The circuit simulator applies FCS individually for each subcircuit concerned by the present state of the circuit. The waveforms of the circuits are partitioned across subcircuits and determined by each solver according to the initial conditions of the passive circuit component (at the time of entering the circuit state), and to the timings of ADC and next switching events. At the effective time of switching, the state of the circuit is updated according to the controller output, leading to different active subcircuits. The solvers associated with these subcircuits are then used for the following simulation step, until a new switching event occurs. The initial state conditions $\vec{X}(0)$ of the circuit is used to estimate weights $\vec{\alpha}$ from (35). For subsequent time events following the change of circuit, the state waveforms $\vec{X}(t)$ is determined using (37). Optionally, all other circuit waveforms $\vec{x}(t)$ may get computed using (36).

D. Timing of Switching Events

Switching of current path in active device is typically delayed compared to the switching events computed with PWM rules. Such delays of actual switching events can be predicted.

Significant delays (few microseconds) may occur during deadtime between top and bottom switches. Conduction may even get interrupted during deadtimes in discontinuous current mode (DCM), as analyzed in [19].

Smaller delays result from the gate driver settings (e.g., high and low gate voltage levels, gate resistance), timings of turn-ON and turn-OFF may vary with operation condition. In high switching frequency applications, mismatched delays affect the effective duty cycle, possibly impacting the stabilization of the control. This behavior can get replicated with accuracy through appropriate lookup tables, derived from DPT results.

V. Circuits With Rotating Machines

Previous section showed the possibility to automate the analysis of power electronic circuits composed of passive *RLC* and active switch devices. Yet, similar analysis method is equally applicable to motor drive circuits including rotating machines.

A. Foreword on Matrix Decomposition

The following algebraic properties will be used later in this section for the analysis of motor drive circuits.

Any matrix $\boldsymbol{A}(s)$ can decomposed as the sum of two matrices of different kinds, parallel $\boldsymbol{A}_{\parallel}(s)$ and antiparallel $\boldsymbol{A}_{\perp}(s)$

$$\boldsymbol{A}_{\parallel}(s)=\begin{bmatrix} a_{\parallel}(s) & b_{\parallel}(s) \\ -b_{\parallel}(s) & a_{\parallel}(s) \end{bmatrix} \; ; \; \boldsymbol{A}_{\perp}(s)=\begin{bmatrix} a_{\perp}(s) & b_{\perp}(s) \\ b_{\perp}(s) & -a_{\perp}(s) \end{bmatrix} . \tag{38}$$

As example, rotation matrix $\boldsymbol{M}(t)$ is of parallel type

$$\boldsymbol{M}(t)=\begin{bmatrix} \cos(\omega t) & \sin(\omega t) \\ -\sin(\omega t) & \cos(\omega t) \end{bmatrix} . \tag{39}$$

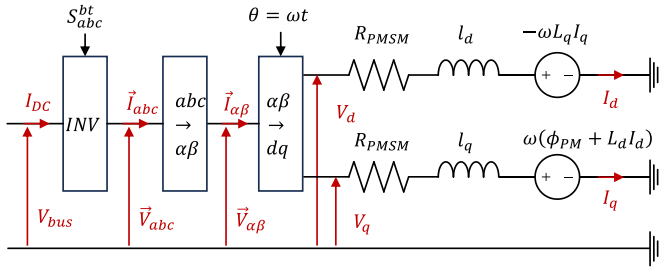

Fig. 5. Electrical model of motor drive (inverter and PMSM).

The product of rotation matrix $\boldsymbol{M}(t)$ has different commutation behaviour with $\boldsymbol{A}_{\parallel}(s)$ and $\boldsymbol{A}_{\perp}(s)$

$$\begin{cases} \boldsymbol{M}.\boldsymbol{A}_{\parallel}(s) = \boldsymbol{A}_{\parallel}(s - \omega\boldsymbol{J}).\boldsymbol{M} \\ \boldsymbol{M}.\boldsymbol{A}_{\perp}(s) = \boldsymbol{A}_{\perp}(s - \omega\boldsymbol{J}).\boldsymbol{M}^{-1} \end{cases}. \tag{40}$$

B. Motor Modeling

Let us now consider a traction drive circuit, with a PMSM modeled by its impedance equation

$$\vec{V}_{dq} - \vec{V}_{PM} = \boldsymbol{Z}_{dq}(s).\vec{I}_{dq} \tag{41}$$

where $\vec{I}_{dq}, \vec{V}_{dq}$ are current and voltage vectors in dq frame, $\vec{V}_{PM}$ is the back electromagnetic force vector resulting from the presence of the magnet flux linkage ϕ_{PM}, and $\boldsymbol{Z}_{dq}(s)$ is machine impedance matrix

$$\boldsymbol{Z}_{dq}(s) = R + \boldsymbol{J}.\boldsymbol{L}.\omega + \boldsymbol{l}.s \tag{42}$$

$$\boldsymbol{J} = \begin{bmatrix} 0 & -1 \\ 1 & 0 \end{bmatrix}; \boldsymbol{L} = \begin{bmatrix} L_d & 0 \\ 0 & L_q \end{bmatrix}; \boldsymbol{l} = \begin{bmatrix} l_d & 0 \\ 0 & l_q \end{bmatrix}. \tag{43}$$

$\boldsymbol{L}$ and $\boldsymbol{l}$ are chord and incremental inductances matrices that differ due to saturation conditions of the machine, ω is the electric pulsation associated to mechanical rotation.

The question of solving the expression of motor current waveforms $\vec{I}_{dq}(t)$ relates to the formulation of motor supplied voltage $\vec{V}_{dq}(t)$. $\vec{V}_{dq}$ is related to circuit voltage vector $\vec{V}_{\alpha\beta}$ in stator frame through Park transformation, using rotation matrix $\boldsymbol{M}(t)$

$$\vec{V}_{dq} = \boldsymbol{M}(t).\vec{V}_{\alpha\beta}. \tag{44}$$

As shown in Fig. 5, the voltage waveform $\vec{V}_{\alpha\beta}$ results from waveforms in *abc* frame through Concordia transformation and is a simple function of the dc-bus voltage V_{bus} and of inverter state S^{bt}_{abc}.

C. Connection of Motor to Electrical Circuit

From (18), the automated analysis of electric drive circuit ultimately leads to a simplified expression

$$\vec{E}_{\alpha\beta} - \vec{V}_{\alpha\beta} = \boldsymbol{Z}_{\alpha\beta}(s).\vec{I}_{\alpha\beta}. \tag{45}$$

Combining (41), (44) and (45), the differential equation driving $\vec{I}_{dq}$ expression becomes

$$\left(\boldsymbol{Z}_{dq}(s) - \boldsymbol{M}.\boldsymbol{Z}_{\alpha\beta}(s).\boldsymbol{M}^{-1}\right).\vec{I}_{dq} = \vec{Y}(t). \tag{46}$$

The excitation waveform $\vec{Y}(t)$ is independent of circuit waveforms and only depends on the back electro-motive force $\vec{V}_{PM}$ of the magnets, on the voltage sources $\vec{E}_{\alpha\beta}$ of the drive circuit, and the rotation matrix $\boldsymbol{M}(t)$ of the machine

$$\vec{Y}(t) = \boldsymbol{M}(t).\vec{E}_{\alpha\beta} - \vec{V}_{\text{PM}}. \tag{47}$$

The problem of formalizing an analytic solution $\vec{I_{dq}}(t)$ from (46) looks very similar to (16) expressed in previous section. A difficulty is however brought by the time-varying impedance term $\boldsymbol{M}.\boldsymbol{Z}_{\alpha\beta}(s).\boldsymbol{M}^{-1}$.

1) Balanced Phase Impedance Circuits: When circuit is symmetric, $\boldsymbol{Z}_{\alpha\beta\perp}(s) = 0$ and $\boldsymbol{Z}_{\alpha\beta}(s) = \boldsymbol{Z}_{\alpha\beta\parallel}(s)$. From (40), the driving differential (46) becomes

$$\boldsymbol{C}(s).\vec{I_{dq}} = \vec{Y}(t) \tag{48}$$

where $\boldsymbol{C}(s) = \boldsymbol{Z}_{dq}(s) + \boldsymbol{Z}_{\alpha\beta}(s - \omega\boldsymbol{J})$ is now a time invariant impedance matrix. Similarly to SSA, such equation system gets elegantly resolved in dq framework as

$$\vec{I_{dq}}(t) = \boldsymbol{C}(s)^{-1}.\vec{Y}(t) + \sum_k \alpha_k.e^{\lambda_k t}.\vec{V_i} \tag{49}$$

where $\boldsymbol{C}(\lambda_k).\vec{V_k} = 0$. Characteristic frequencies $\{\lambda_k\}$ verify $det\ (\boldsymbol{C}(\lambda)) = 0$. Characteristic vector $\vec{V_k}$ is eigenvector corresponding to zero eigen value of matrix $\boldsymbol{C}(\lambda_k)$, and weights $\vec{\alpha}$ are determined from initial conditions

$$\vec{\alpha} = \boldsymbol{V}^{-1}.\left(\vec{I_{dq}}(0) - \boldsymbol{C}(s)^{-1}.\vec{Y}(0)\right). \tag{50}$$

Ultimately, motor currents are determined in stator framework $\vec{I_{\alpha\beta}}(t)$

$$\vec{I_{\alpha\beta}} = \boldsymbol{M}(t)^{-1}.\vec{I_{dq}}(t). \tag{51}$$

2) Nonsalient Pole Machines: When machine is nonsalient, $L_d = L_q = L$, $l_d = l_q = l$, the machine impedance matrix becomes of parallel type so that $\boldsymbol{Z}_{dq\perp}(s) = 0$ and $\boldsymbol{Z}_{dq}(s) = \boldsymbol{Z}_{dq\parallel}(s)$

$$\boldsymbol{Z}_{dq}(s) = (R + ls).\boldsymbol{I} + \boldsymbol{J}.\boldsymbol{L}.\omega. \tag{52}$$

Then, using (40), the driving differential (46) can be rewritten as

$$\boldsymbol{C}(s).\vec{I_{\alpha\beta}} = \boldsymbol{M}^{-1}.\vec{Y} \tag{53}$$

where $\boldsymbol{C}(s) = \boldsymbol{Z}_{dq}\ (s - \omega\boldsymbol{J}) + \boldsymbol{Z}_{\alpha\beta}(s)$ is a time-invariant impedance matrix. Such equation system gets elegantly resolved in $\alpha\beta$ framework as

$$\vec{I_{\alpha\beta}}(t) = \boldsymbol{C}(s)^{-1}.\boldsymbol{M}^{-1}.\vec{Y} + \sum_k \alpha_k.e^{\lambda_k t}.\vec{V_k} \tag{54}$$

where $\boldsymbol{C}(\lambda_k).\vec{V_k} = 0$. Characteristic frequencies $\{\lambda_k\}$ verify $\det\ (\boldsymbol{C}(\lambda)) = 0$.

3) General Case: As the circuit impedances seen from motor phases vary with switching conditions, they are necessarily unbalanced at least in some of the inverter states.

Unfortunately, for salient-pole machines fed with such unbalanced circuit impedances, (46) no longer represents an ODE system with constant coefficients, and its solution can no longer

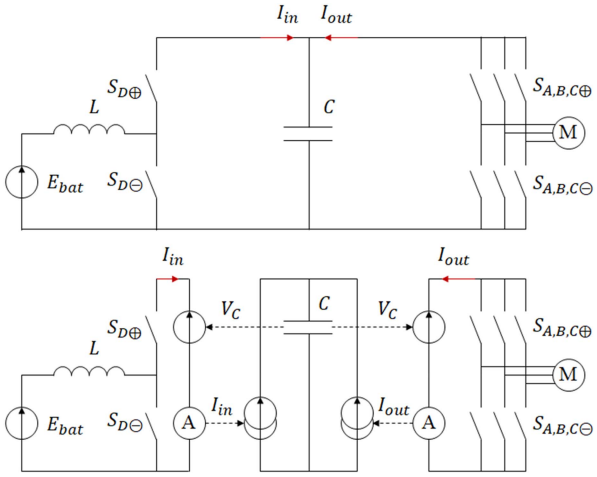

Fig. 6. Simulation of (a) traction chain combining DC/DC Boost converter and three-phase Inverter traction chain using and (b) split circuits.

get determined as a closed-form expression built from exponential functions.

In absence of closed-form expression, solutions could be approximated by polynomial functions. The associated approximation error might be kept below a target accuracy amid computational costs resulting from large truncation orders and/or reduced simulation step.

4) Work-Around for Salient Machines: To keep advantages of closed-form expression of waveforms for motor drive circuits controlling salient-pole machines, a possible way forward consists in splitting the motor drive circuit into three unconnected parts.

In the split representation shown in Fig. 6, the input and output stages are connected to voltage sources representative of the dc bus, and the dc-bus stage is connected to current sources, representative of currents flowing in input and output stages.

Input and output stages are solved separately to determine the current waveforms flowing to/from the dc bus. As the machine is fed using voltage source instead of capacitance, the phase impedances can be regarded as balanced across phases, and formulation (49) applies. Then, dc-bus stage is simulated by integration of current waveforms obtained in the input and output stages.

Both input and output stages are solved using closed-form solutions. The split method enables the simulation of small variations on the dc-bus voltage, as the bus capacitor voltage is updated from the current of both input and output stage at each simulation event (ADC sampling, switching events)

$$V_C(t+\Delta t) = V_C(t) + \frac{C}{\Delta t}\int_0^{\Delta t} (I_{in} + I_{out})\, dt. \tag{55}$$

The average current flown during time interval Δt can get precisely formulated from current expression given by (54)

$$\frac{1}{\Delta t}\int_0^{\Delta t} \left(\alpha_0 + \sum \alpha_k . e^{\lambda_k t}\right) dt = \alpha_0 + \sum \alpha_k . \frac{e^{\lambda_k \Delta t} - 1}{\lambda_k . \Delta t}. \tag{56}$$

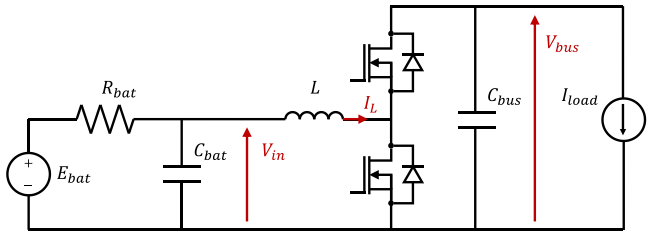

Fig. 7. Circuit configuration for the verification of simulation concept (DC/DC converter).

TABLE I
PARAMETERS FOR VERIFICATION OF SIMULATION CONCEPT

Parameter	Value	Parameter	Value
E_{bat}	200 V	V^*_{bus}	650 V
R_{bat}	50 $m\Omega$	L	170 μH
R_L	50 $m\Omega$	C_{bat}	250 μF
I_{load}	$100/-100A$	C_{bus}	850 μF
f_{switch}	10 kHz	f_{CTRL}	20 kHz
deadtime	4μs	k_I	0.1s

While input and output stages may be controlled independently with different control and switching frequencies, all stages are simulated at same timing events, collecting sampling and switching events of both controllers.

On the output stage, the input circuit (45) derates as $\vec{V}_{\alpha\beta} = \vec{E}_{\alpha\beta}$ where $\vec{E}_{\alpha\beta}$ only depends on inverter state and on voltage level V_{DC} dc source. As $\boldsymbol{Z}_{\alpha\beta}(s) = 0$, the formulation of Laplace matrix $\boldsymbol{C}(s)$ is simplified as

$$\boldsymbol{C}(s) = \boldsymbol{Z}_{dq}(s) = \begin{bmatrix} R + l_d s & -\omega L_q \\ \omega L_d & R + l_q s \end{bmatrix}. \tag{57}$$

The characteristic frequencies of the machine are reached from $\det(\boldsymbol{C}(\lambda)) = 0$ criterion

$$\lambda_k = \frac{-R(l_d + l_q) \pm R(l_d - l_q)\sqrt{1 - \frac{4\omega^2 l_d l_q L_d L_q}{R^2 (l_d - l_q)^2}}}{2 l_d l_q}. \tag{58}$$

The characteristic eigenvector vectors associated to each characteristic frequency of the motor are given by

$$\vec{V}_k = \begin{bmatrix} R + l_q \lambda_k \\ -\omega L_d \end{bmatrix}. \tag{59}$$

VI. VERIFICATION OF FCS PERFORMANCE

A. Step-Up DC/DC Converter

In a first example shown in Fig. 7 and Table I, a bidirectional dc/dc boost chopper is fed by a battery and aims at delivering higher dc voltage to a load with regeneration capability. The load is symbolized as a controllable current source. The circuit controller decides the activation timing of the unique half bridge to steer the dc-bus voltage to some predetermined dc-bus voltage. Switching frequency was set to 5 kHz, and controller operates at 10 kHz, with dc-bus voltage sampled at both edges of PWM carrier. The duty cycle of the half bridge is controlled by an integral regulator to steer the capacitor voltage to the desired regulation voltage.

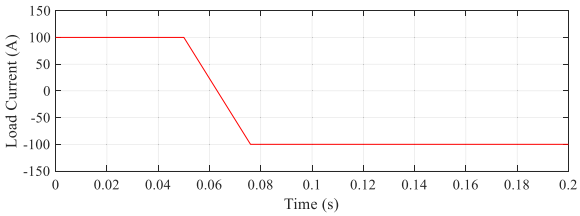

Fig. 8. Reversal of controllable load current source.

As shown in Fig. 8, at $t = 0.05$ s, the load current source I_{load}changes from power consumption mode to power regeneration mode. During the power ramp period, the energy collected in the passive energy storage device must adapt to new levels, causing an inevitable overshoot in dc-bus voltage $V_{C\text{bus}}$. Such overshoot may be harmful to the design of the dc/dc converter and needs to get evaluated with accuracy.

The verification of this power reversal scenario was realized with proposed fast circuit simulation (FCS) and compared with the results of commercial circuit simulation tool (PSIM [5]). Waveform results are gathered in Figs. 9. Left side of Fig. 9 shows all simulation steps evaluated using the fixed-step commercial simulation tool. In contrast in right side, FCS computed the waveforms only at timings of following events: switching timings decided by controller (CTRL events), sampling events (ADC events), end of deadtimes (DT events), and possibly zero-crossing events (ZC/DCM events) during deadtimes. With both simulators, the circuit exhibits secondary overshoots amplified by the duration of deadtime, with DCM occurrence when the inductor current i_L enters (around $t = 0.06$ s) and leaves (around $t = 0.07$ s) the zero-current area, as indicated in Fig. 9 by the presence of zero-crossing DCM events. To replicate such secondary overshoot with accuracy, the simulation of precise behavior of DCM in such situation typically requires a high precision on the simulation step, which should be typically much smaller than the deadtime.

Fig. 10 shows the differences in the results obtained with commercial simulation software under different timesteps versus results reached with proposed approach, around the main peak in dc-bus voltage overshoot. The observed differences not only lie in the accuracy of waveform prediction between two simulation steps:

1) It also lies in the setting of switching timings. In conventional simulators, the granularity of the control and switching timing (including deadtime and zero-crossing) is necessarily set by the simulation step.
2) Between simulation steps surrounding a zero crossing, the simulated circuit behavior is ambiguous as the circuit state is not clearly defined in that period.
3) In conventional simulation tool, the linear nature of time piecewise linear current source is also neglected and translated into as multistep current source, affecting the accuracy.
4) The controller response to waveform inaccuracy causes changes in duty cycles, also causing supplemental marginal errors.

TABLE II
COMPARISON OF SIMULATORS FOR DC/DC BOOST CIRCUIT

Simulator	Number of simulation steps	Elapsed CPU time	Peak V_{bus} Level (V)
Fast Circuit Solver	6028	97 ms	734.9
1us fixed step	2e5	1s	730.2
100ns fixed step	2e6	8s	734.4
10ns fixed step	2e7	98s	734.8

TABLE III
PARAMETERS OF EVALUATED MOTOR DRIVE

Parameter	Value	Parameter	Value
ϕ_{PM}	50 mVs	$N_{polepairs}$	4
L_d	100 µH	l_d	100 µH
L_q	250 µH	l_q	150 µH
R_{PMSM}	10 mΩ	V_{bus}	290 V
ω	4000 rpm	T	200 Nm
f_{sw}	5 KHz	f_{CTRL}	10 KHz

CPU results gathered in Table II confirm that the truncation error of fixed-step simulator gets reduced with smaller fixed simulation step, and the results of fixed step simulator progressively converge towards FCS results, that are free of any approximation. To near the inherent accuracy of FCS simulation, fixed timestep must get significantly reduced, with major impairment on CPU complexity. To reach similar asymptote accuracy, the elapsed CPU time was reduced by several orders of magnitudes (∼1/1000) compared with linear solver and fixed simulation step. The reduction of CPU complexity is heavily driven by the reduction in the number of simulation steps. FCS simulation over 200 ms simulation time took 97 ms CPU time on i7-1265U/1.8 GHz laptop, showing the potential of the method for real-time implementation or for simulation-in-the-loop, just using standard computing unit and interpreted programming language. FCS was implemented as a MATLAB interpreted routine, and elapsed CPU time was therefore not optimized, in contrast to compiled commercial software. FCS would largely benefit from additional CPU gain using e.g., compiled C++ implementation without need for hardware implementation (e.g., FPGA).

B. PMSM Drive With Stabilized DC Source

In this second example case, the investigated motor drive circuit is composed of only the output stage of Fig. 6, where three-phase inverter is fed with a stabilized dc voltage source and controlled under constant rotational speed with Field Oriented Control, shown in Fig. 11. Parameters of motor drive are collected in Table III. The machine impedances are linearized around maximum-torque-per-ampere operation condition.

As seen in Fig. 12, proposed simulation method perfectly reproduces PWM details of phase current waveforms, while the number of simulation steps was drastically reduced by a ratio 10 000, compared with 10ns fixed-step simulation.

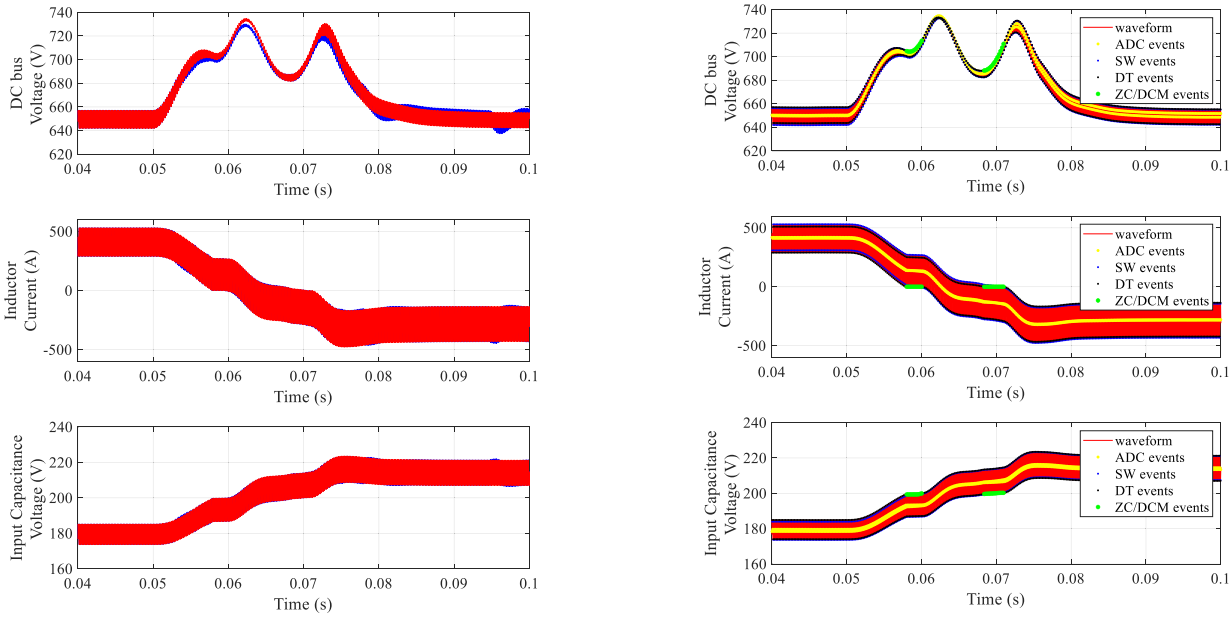

Fig. 9. Comparison of circuit waveforms (left) fixed simulation step (blue : 1 μs red : 10 ns) versus (right) fast circuit simulator (FCS).

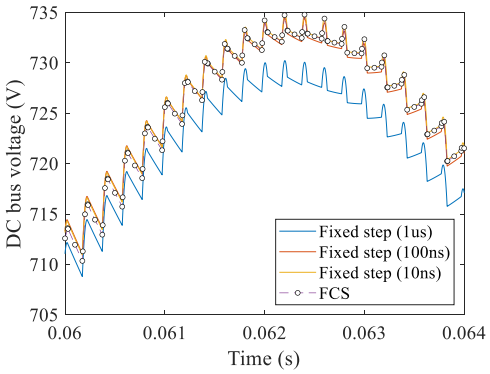

Fig. 10. Comparison of detailed circuit waveform using FCS versus commercial simulation software with different simulation steps.

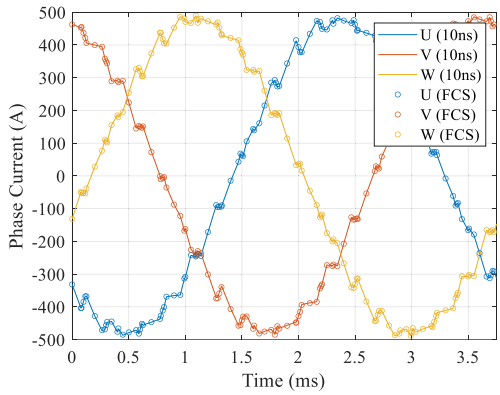

Fig. 12. Comparison of simulated current waveforms of a traction chain combining stabilized DC-bus voltage source, three-phase PWM inverter, and PMSM.

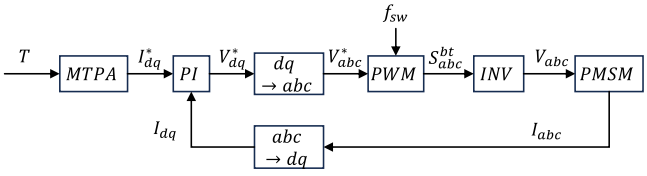

Fig. 11. Field oriented controller (FOC).

C. PMSM Drive With Battery and DC/DC Converter

The proposed analysis method was then also verified for the salient / unbalanced phase impedance case, investigated in our last example. The studied motor drive circuit is composed of dc/dc converter (from our first example, Fig. 7) coupled to inverter/PMSM drive circuit (from our second example) through a stronger dc bus (650 V instead of 290 V). The simulation was realized with FCS according to the proposed work-around using split circuits. DC/DC converter and inverter are operated with individual control and switching frequencies.

Fig. 13 shows the simulated waveforms with conventional circuit simulator and with FCS. For both simulators, the power circuit was configured with initial conditions expected at steady state, while internal variables of controllers were configured with arbitrary misconfigured values. Poor configuration of controller produces shaken behavior of circuit waveforms until controllers reach steady state again. This behavior applies with both simulators, showing that the proposed work-around method can precisely replicate the oscillations of dc-bus voltage caused by the combination of currents flowing from both dc/dc chopper and inverter circuits. Although FCS computes waveforms only at ADC and switching events, the obtained time-domain waveforms properly replicate the ripple details observed with fixed-step simulation.

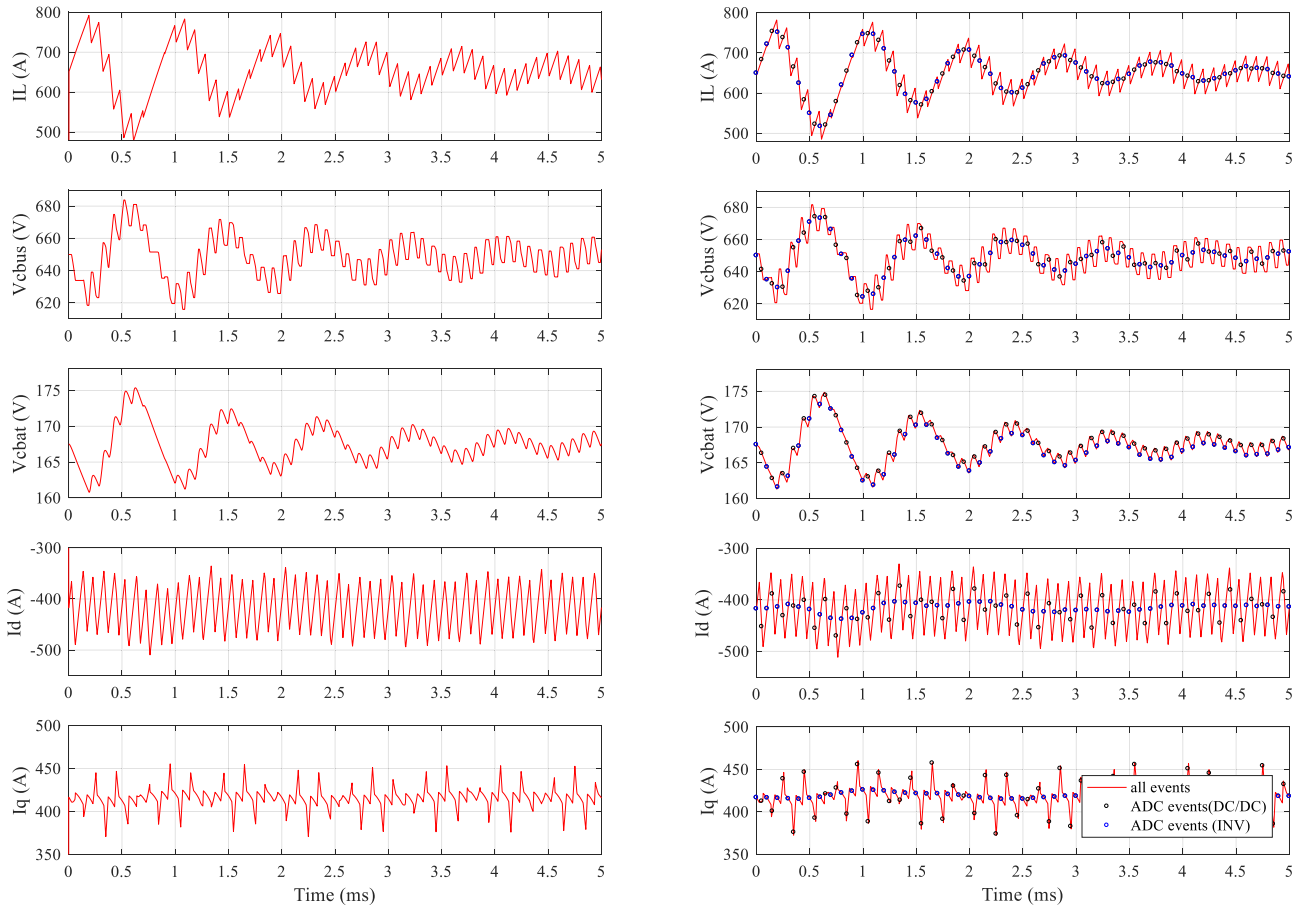

Fig. 13. Simulated waveforms of (DC/DC + INV + PMSM) circuit. (a) With fixed 1 μs simulation step. (b) With FCS.

The computation of average bus capacitor current (56) slows down FCS, that no longer meets the faster-than-real-time criterion. FCS simulation over 100 ms took 7s CPU time, still much less than the 269s CPU time measured with commercial simulator. The acceleration factor is thus less in motor drive application, but still of significant interest for steady state simulations.

In contrast, speed-transient simulation with variable speed and/or torque would be further slowed down, as initialization step shown in Fig. 2 (identification of characteristic frequencies from (58), of eigen vectors (59), and inversion of matrix $\boldsymbol{V}$) must regularly be recomputed to meet instant speed/inductance conditions, as speed ω_e and inductances L_d, L_q, l_d, l_q may vary according to nonlinear saturation.

VII. Conclusion

Simulation of power electronic circuit can be greatly accelerated using closed-form expression of its waveforms as function of time: waveforms are directly expressed at the event timings of interest, skipping the need for evaluation at intermediate simulation steps. The formal solutions are expressed as a weighted sum of exponential functions of time. The formulation is exact and free of any truncation approximation. The precise formulation of complex characteristics frequencies and weights can get determined from either SSA or MNA formalisms and for any linear circuit.

This article explored and showed the extension of proposed FCS principles to motor drive circuits that combine dc/dc converter, three-phase inverter and a rotational PMSM machine. For salient machines where the solution waveforms may no longer take an exponential analytical form, a workaround was proposed and shown effective in reproducing circuit waveforms with reasonable accuracy. For each evaluation case, the proposed fast circuit simulation method could drastically reduce the number of simulation steps and the elapsed CPU time, compared with existing commercial simulation software. CPU performance will get further improved using compiled software rather than interpreted software. The proposed FCS structure can address steady state operation of motor drive at constant torque $\times$ speed operation points, and this is possibly sufficient to evaluate in a short time the performance of the drive on large automotive or railway mission profiles.

More investigation is necessary to fully assess with FCS the dynamic performance (e.g., stiff response to torque steps and/or speed ramp) of motor drive controllers for other demanding applications such as servo drives.

Frequency-domain analysis may be applied offline to FCS waveforms, through waveform interpolation at regular time

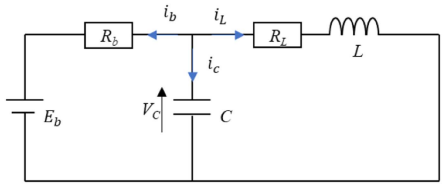

Fig. 14. Example circuit.

intervals before application of Fourier analysis. This method is however not suited for frequencies much higher than the switching frequency. In principles, the application of FCS solver for EMC tones associated to switching transients may be possible but deserves to be investigated in full details, with specific challenges related to the nonlinearities of circuit parameters in switching device models.

The approach is very promising for accelerating simulation time and may enable new usages of real-time simulation in embedded applications, e.g., simulation-in-the-loop, digital twins, or model-predicted control.

Appendix: Example Circuit

For the sake of clarity, the proposed approach is exemplified in the simple circuit shown in Fig. 14, where a battery voltage source is connected to a capacitor connected in parallel to an inductor.

The circuit waveform vector is given by $\vec{x} = (V_c, i_b, i_c, i_L)^T$. For this circuit with $N_P = 2$, $N_b = 3$, $N_n = 2$, and the $\boldsymbol{C}$, $\boldsymbol{G}$ matrices representing the MNA equation system (2) have the following contents:

$$\boldsymbol{C} = \begin{bmatrix} C & 0 & 0 & 0 \\ 0 & 0 & 0 & L \\ 0 & 0 & 0 & 0 \\ 0 & 0 & 0 & 0 \end{bmatrix}; \boldsymbol{G} = \begin{bmatrix} 0 & 0 & -1 & 0 \\ -1 & 0 & 0 & R_L \\ 1 & -R_b & 0 & 0 \\ 0 & 1 & 1 & 1 \end{bmatrix}; \vec{u} = \begin{bmatrix} 0 \\ 0 \\ E_b \\ 0 \end{bmatrix}$$

$$\boldsymbol{C} = \begin{bmatrix} \Delta.K \\ 0 \end{bmatrix} \text{ with } \boldsymbol{K} = \begin{bmatrix} 1 & 0 & 0 & 0 \\ 0 & 0 & 0 & 1 \end{bmatrix} \text{ and } \boldsymbol{\Delta} = \begin{bmatrix} C & 0 \\ 0 & L \end{bmatrix}. \tag{60}$$

The Laplace matrix $\boldsymbol{A}_{\text{MNA}}(s)$ in (16) takes the form

$$\boldsymbol{A}_{\text{MNA}}(s) = \begin{bmatrix} Cs & 0 & -1 & 0 \\ -1 & 0 & 0 & R_L + Ls \\ 1 & -R_b & 0 & 0 \\ 0 & 1 & 1 & 1 \end{bmatrix}. \tag{61}$$

Using (18), the result of triangulation of $\boldsymbol{A}_{MNA}(s)$ brings $\boldsymbol{D}(s).\vec{x} = \vec{V}$ with

$$\boldsymbol{D}(s) = \begin{bmatrix} 1 & 0 & 0 & -(R_L + Ls) \\ 0 & 1 & 0 & 1 + (R_L + Ls)Cs \\ 0 & 0 & 1 & -(R_L + Ls)Cs \\ 0 & 0 & 0 & 1 \end{bmatrix} \tag{62}$$

$$\vec{V} = \frac{1}{R_b + R_L + Ls + R_b R_c Cs + R_b LCs^2} \begin{bmatrix} 0 \\ 0 \\ 0 \\ E_b \end{bmatrix}. \tag{63}$$

Quotient polynomial $Q(s) = R_b + R_L + Ls + R_b R_c Cs + R_b LCs^2$ has 2 complex roots λ_1 and λ_2 verifying $Q(\lambda) = 0$. In this example, roots are analytically identified as

$$\lambda_{1,2} = \frac{-L - R_b R_c C \pm \sqrt{(L + R_b R_c C)^2 - 4(R_b + R_L) R_b LC}}{2R_b LC}. \tag{64}$$

From $\boldsymbol{D}(s)$ expression, the transfer functions between each waveform and the last waveform $i_L(t)$ are identified as

$$\begin{cases} F_1(s) = \frac{V_c}{i_L} = R_L + Ls \\ F_2(s) = \frac{i_b}{i_L} = -1 - (R_L + Ls) Cs \\ F_3(s) = \frac{i_c}{i_L} = (R_L + Ls) Cs \\ F_4(s) = i_L / i_L = 1 \end{cases}. \tag{65}$$

Finally the matrix $\boldsymbol{K}.\boldsymbol{F}$ used for the computation of weights (35), of the circuit waveforms (36) and of the passive waveforms (37) comes as

$$\boldsymbol{K}.\boldsymbol{F} = \boldsymbol{K}. \begin{bmatrix} F_1(\lambda_1) & F_1(\lambda_2) \\ F_2(\lambda_1) & F_2(\lambda_2) \\ F_3(\lambda_1) & F_3(\lambda_2) \\ F_4(\lambda_1) & F_4(\lambda_2) \end{bmatrix} = \begin{bmatrix} R_L + L\lambda_1 & R_L + L\lambda_2 \\ 1 & 1 \end{bmatrix}. \tag{66}$$

References

[1] "Worldwide harmonised light-duty vehicles test procedure (WLTP) and real driving emissions (RDE)". European Commission, 2017. [Online]. Available: https://eur-lex.europa.eu/EN/legal-content/summary/worldwide-harmonised-light-duty-vehicles-test-procedure-wltp-and-real-driving-emissions-rde.html

[2] "Railway Applications - Rolling stock - Specification and verification of energy consumption," EN 50591, CENELEC, 2019.

[3] I. Martinez et al., "A multi-physics approach for minimising motor losses on the WLTP driving cycle," in *Proc. 11th Int. Conf. Power Electron., Mach. Drives*, 2022, pp. 34–40, doi: 10.1049/icp.2022.1011.

[4] M. Hepp, L. Hertenstein, A. Nisch, W. Wondrak, F. Bertele, and M. Heller, "Potential of GaN Semiconductors in electric vehicle inverters," in *Proc. PCIM Eur. Int. Exhib. Conf. Power Electron., Intell. Motion, Renew. Energy Energy Manage.*, 2022, pp. 1–8, doi: 10.30420/565822134.

[5] "PSIM user manual" Version 2012, Powersim Inc., 2020, [Online]. Available: https://powersimtech.com/support/resources/tutorials/psimuser-manual/

[6] "PLECS user manual" Version 4.2, Plexim GmbH, 2018. [Online]. Available: https://www.plexim.com/download/documentation

[7] Y. Zhu, Z. Zhao, B. Shi, and Z. Yu, "Discrete state event-driven framework with a flexible adaptive algorithm for simulation of power electronic systems," *IEEE Trans. Power Electron.*, vol. 34, no. 12, pp. 11692–11702, Dec. 2019.

[8] B. Shi, Z. Zhao, Y. Zhu, Z. Yu, and J. Ju, "Discrete state event-driven simulation approach with a state-variable-interfaced decoupling strategy for large-scale power electronics systems," *IEEE Trans. Ind. Electron.*, vol. 68, no. 12, pp. 11673–11683, Dec. 2021, doi: 10.1109/TIE.2020.3044804.

[9] L. Yongtao, C. Jianan, and J. Dong, "Comparison and analysis of DSIM and SIMULINK simulation based on MMC system," in *Proc. IEEE 4th Int. Elect. Energy Conf.*, 2021, pp. 1–6, doi: 10.1109/CIEEC50170.2021.9510501.

[10] C.-W. Ho, A. Ruehli, and P. Brennan, "The modified nodal approach to network analysis," *IEEE Trans. Circuits Syst.*, vol. 22, no. 6, pp. 504–509, Jun. 1975.
[11] D. Rowell, "Time-domain solution of LTI state equations," 2002. [Online]. Available: https://web.mit.edu/2.14/www/Handouts/StateSpaceResponse.pdf
[12] "Simulink user's guide," Version R2020a, Mathworks, 2020. [Online]. Available: https://www.mathworks.com/help/pdf_doc/simulink
[13] J. Ju, Z. Zhao, B. Shi, Y. Zhu, and Z. Yu, "Motor-oriented discrete state event-driven method for multitime-scale simulation of power traction systems," *IEEE Trans. Transp. Electrific.*, vol. 7, no. 3, pp. 1652–1661, Sep. 2021, doi: 10.1109/TTE.2021.3053027.
[14] P. J. van Duijsen, "Steady-state analysis and sampled data modeling of AC power converters using the MNA method. (modified nodal analysis)," in *Proc. 5th Eur. Conf. Power Electron. Appl.*, 1993, vol. 5, pp. 157–162.
[15] L. Brančík, "Modified nodal analysis and state variable descriptions for MTLs systems solution in Matlab," in *Proc. 36th Int. Conf. Telecommun. Signal Process.*, 2013, pp. 354–357, doi: 10.1109/TSP.2013.6613951.
[16] C. Hao and M. Merlin, "Automatic derivation of state-space model from linear electrical circuits with dependent variables using modified nodal analysis," in *Proc. IEEE 21st Workshop Control Model. Power Electron.*, 2020, pp. 1–6, doi: 10.1109/COMPEL49091.2020.9265762.
[17] M. Shenk, "AnSim: An analytic simulator for electronic circuits," Ph.D. dissertation, Graz Univ. Technol., Graz, Austria, 2020.
[18] S. J. Mason, "Feedback theory-some properties of signal flow graphs," *Proc. IRE*, vol. 41, no. 9, pp. 1144–1156, Sep. 1953.
[19] N. Voyer, A. Nakabayashi, and R. Kondo, "Fast circuit simulation of linear electronic circuits using modified nodal analysis," in *Proc. IEEE Energy Convers. Congr. Expo.*, 2024, pp. 3825–3832.
[20] T. Cheng, D. Dah-ChuanLu, and Y. P. Siwakoti, "Electro-thermal average modeling of a boost converter considering device self-heating," in *Proc. IEEE Appl. Power Electron. Conf. Expo.*, 2020, pp. 2854–2859.

N. Voyer received the engineering degree in digital communication from Telecom ParisTech, Paris, France, in 1995.

From 1997 to 2008, as a Research Engineer with Mitsubishi Electric Information Technology Europe, Rennes, France, he contributed to the standardization of 3G/4G mobile cellular networks in 3GPP. In 2008, he became a Research Manager in Power Electronics Systems Division, Mitsubishi Electric Research Centre Europe, presently acting as a Chief Scientist. He is an Co-Inventor of more than 90 patents. His research interests include the control, design, modeling, and diagnosis of power electronics systems, such as PV, railway and EV traction, HVDC.

A. Nakabayashi received the M.S. degree in maritime science and technology from Kobe University, Kobe, Japan, in 2015.

Since 2015, she has been Mitsubishi Electric Corporation, Amagasaki, Japan. Her research focuses on the control of power converters.

R. Kondo (Senior Member) received the M.S degrees in electrical engineering from the Tokyo Institute of Technology, Tokyo, Japan, in 2009, and the Ph.D. degree in electrical engineering from Osaka University, Osaka, Japan, in 2023, respectively.

Since 2009, he has been Mitsubishi Electric Corporation, Amagasaki, Japan. From 2017 to 2019, he was a Visiting Researcher of RWTH Aachen University, Aachen, Germany. His research interests include circuit topology and converter design modeling.

Dr. Kondo is a Senior Member of IEEE.